ON SEA ICE CHARACTERISATION BY MULTI-FREQUENCY SAR

Jakob Grahn[1], **Camilla Brekke**[1], **Torbjørn Eltoft**[1], **and Benjamin Holt**[2]

[1]*Department of Physics and Technology, University of Tromsø, 37191 Tromsø, Norway*
[2]*Jet Propulsion Laboratory, California Institute of Technology, CA 91109 Pasadena, United States*

ABSTRACT

By means of polarimetric target decomposition, quad-pol SAR data of sea ice is analysed at two frequency bands. In particular, the non negative eigenvalue decomposition (NNED) is applied on L- and C-band NASA/JPL AIRSAR data acquired over the Beaufort sea in 2004. The decomposition separates the scattered radar signal into three types, dominated by double, volume and single bounce scattering respectively. Using ground truth derived from RADARSAT-1 and meteorological data, we investigate how the different frequency bands compare in terms of these scattering types. The ground truth contains multi year ice and three types of first year ice of different age and thickness.

We find that C-band yields a higher scattered intensity in most ice and scattering types, as well as a more homogeneous intensity. L-band on the other hand yields more pronounced deformation features, such as ridges. The mean intensity contrast between the two thinnest ice types is highest in the double scattering component of C-band, although the contrast of the total signal is greater in L-band. This may indicate that the choice of polarimetric parameters is important for discriminating thin ice types.

Key words: Image processing; Polarimetry; Remote sensing; Sea Ice; Multi-frequency; SAR.

1. INTRODUCTION

Sea ice is an integrated part of the polar weather and climate systems as well as of many polar ecosystems. In order to make accurate predictions in these systems, it is important to map certain characteristics of the sea ice. In addition, valid and cost efficient ice mapping services is important to maritime operation in the arctic region, which is increasing along with a decreasing seasonal ice cover.

During the past decades, air and space borne synthetic aperture radar (SAR) has become one of the most commonly used tools for gathering information about Earth's surface. For sea ice mapping, SAR systems operating with frequencies in C-band (wavelengths around 5.6 cm) have conventionally been considered as the overall best choice, if one polarisation is used. However, since the development of polarimetric SAR, having the ability to send and receive pulses at different polarisations, researchers have indicated that the choice of C-band may not always be obvious (see for example [1] and references therein).

By for instance using L-band (wavelengths around 24 cm), it has been shown that some ice types can be more easily discriminated, given multiple polarisations. For example, [2] shows that L-band yield higher contrasts between level ice and deformed ice and [3, 4, 5] shows that multiple ice type classification can have an overall higher accuracy using L-band compared to C-band. Considering thin ice types however, reports seem to differ on wether longer wavelengths are preferable or not, as noted by for example [6].

This motivates us to study the use of multiple frequency bands further and we address the discrimination between multi year (MY) and first year (FY) ice of different age and thickness in particular.

How well different ice types can be discriminated is to some extent a matter representing the SAR data in terms of proper parameters. For polarimetric SAR data, a variety of parameters are commonly used such as co-polarised and co- to cross-polarised ratio, co-polarised phase difference, co-polarised correlation coefficient or pedestal height for example. In this paper, we choose to define the polarimetric parameters in terms of a target decomposition. In particular we employ the non negative eigenvalue decomposition (NNED) by [7] which separates the scattered radar signal into predefined scattering types. The scattering types are chosen following [8], for which they can be interpreted as double bounce, volume and single bounce scattering. This give us the ability to easily visualise the differences between frequency bands in terms of simple scattering mechanisms relating to the structure of the ice types.

The outline of the paper is as follows: first some formalism of radar polarimetry is introduced followed by a description of how the NNED is implemented. The data set and ground truth is presented followed by results acquired by applying the NNED on the data. The paper ends with a short discussion that highlights the major findings.

Proc. 'ESA Living Planet Symposium 2013', Edinburgh, UK
9–13 September 2013 (ESA SP-722, December 2013)

2. RADAR POLARIMETRY

A polarimetric SAR system has the ability to transmit and receive radar waves at different polarisations. By measuring the change in the polarisation between transmitted and received waves, valuable information about the material causing the scattering can be retrieved.

Mathematically, a scattering process can be described as a linear transformation between a transmitted and received wave, commonly expressed in terms of Jones vectors. Here we use the bra-ket notation for the vectors, such that a ket vector $|\boldsymbol{E}\rangle$ is defined as a complex valued column vector and the corresponding bra vector $\langle \boldsymbol{E}|$ is it's conjugate transpose, that is $\langle \boldsymbol{E}| = |\boldsymbol{E}\rangle^{T*}$. The scattering between a transmitted wave $|\boldsymbol{E^{tr}}\rangle$ and a received wave $|\boldsymbol{E^{rec}}\rangle$ is then written as $|\boldsymbol{E^{rec}}\rangle = \mathbf{S}\,|\boldsymbol{E^{tr}}\rangle$, where $\mathbf{S}$ is a 2×2 complex valued scattering matrix. The polarisation basis is typically chosen as horizontal (h) and vertical (v) to the plane of incidence, for which we write the transformation explicitly as

$$\begin{bmatrix} E_h^{rec} \\ E_v^{rec} \end{bmatrix} = \begin{bmatrix} S_{hh} & S_{hv} \\ S_{vh} & S_{vv} \end{bmatrix} \begin{bmatrix} E_h^{tr} \\ E_v^{tr} \end{bmatrix} \tag{1}$$

To fully determine the scattering matrix, the radar must be able to independently transmit and receive in both h and v, in which case it is referred to as quad-pol or fully polarimetric.

For natural targets, the scattering matrix typically turns out to be symmetric, that is $S_{hv} = S_{vh}$. It then reduces to three independent elements and can be written as a scattering vector

$$|\boldsymbol{s}\rangle = \left[S_{hh},\ \sqrt{2}S_{hv},\ S_{vv}\right]^T \tag{2}$$

To further relate the scattering vector to intensities a covariance scattering matrix $\mathbf{C}$ is defined as

$$\mathbf{C} = |\boldsymbol{s}\rangle\,\langle \boldsymbol{s}| \tag{3}$$

The main benefit of expressing the scatterer in terms intensities in the covariance matrix instead of amplitudes in the scattering vector, is that intensities may be averaged over multiple resolution cells in order to reduce speckle noise.

The total intensity I measured by the system is found as [9]

$$I = \langle \boldsymbol{s}|\,|\boldsymbol{s}\rangle = \mathrm{Tr}\{\mathbf{C}\} \tag{4}$$

For a realistic scatterer, the intensity must be positive, which implies that the eigenvalues of the covariance matrix also must be positive [7]. This fact is considered next, when decomposing scatterers into realistic scattering types with the NNED.

3. NNED

The general idea of polarimetric decompositions, is to separate the scatterers into components that are convenient to use or interpret. Here, we consider a model based decomposition of the scattering covariance matrix $\mathbf{C}$, for which it is separated into a linear combination of three model matrices, each corresponding to a predefined scattering type.

Specifically, we follow [8] and consider the model matrices corresponding to double bounce, volume and single bounce scattering:

$$\mathbf{C}^{dbl} = \begin{bmatrix} |d|^2 & 0 & d \\ 0 & 0 & 0 \\ d^* & 0 & 1 \end{bmatrix} \qquad double$$

$$\mathbf{C}^{vol} = \begin{bmatrix} 1 & 0 & 1/3 \\ 0 & 2/3 & 0 \\ 1/3 & 0 & 1 \end{bmatrix} \qquad volume$$

$$\mathbf{C}^{sgl} = \begin{bmatrix} |s|^2 & 0 & s \\ 0 & 0 & 0 \\ s^* & 0 & 1 \end{bmatrix} \qquad single$$

where d and s are complex valued model parameters. The scattering covariance matrix $\mathbf{C}$ is then written as

$$\mathbf{C} = f_{dbl}\mathbf{C}^{dbl} + f_{vol}\mathbf{C}^{vol} + f_{sgl}\mathbf{C}^{sgl} + \mathbf{C}^{rst} \tag{5}$$

where f_{dbl}, f_{vol} and f_{sgl} are scalar weights and $\mathbf{C}^{rst}$ is a rest matrix, containing the part of $\mathbf{C}$ that cannot be expressed by the model matrices (it will for example contain the elements C_{12}, C_{21}, C_{23} and C_{32} of the total covariance matrix, although these are typically small).

The eigenvalues of a covariance matrix must be positive in order to represent a physical scatterer [7] and we thus require that each of the decomposed terms in equation (5) have positive eigenvalues. This can be guaranteed by applying the non-negative eigenvalue decomposition (NNED) introduced in [7]. The procedure can be described in three steps as follows:

1. First the volume term is subtracted from the total covariance matrix, that is

$$\mathbf{C}' = \mathbf{C} - f_{vol}\mathbf{C}^{vol} \tag{6}$$

where f_{vol} is chosen such that the eigenvalues of $\mathbf{C}'$ are minimised, yet positive. Mathematically, it can be shown [7] that this corresponds to

$$f_{vol} = \min \begin{cases} \frac{2}{3}C_{22}^{vol} \\ \frac{9}{16}\left(a\sqrt{|a|^2 - b}\right) \end{cases} \tag{7}$$

where

$$a = C_{11}^{vol} + C_{33}^{vol} - \frac{2}{3}Re\{C_{13}^{vol}\}$$

$$b = \frac{32}{9}C_{11}^{vol}C_{33}^{vol} - |C_{13}^{vol}|^2$$

2. Secondly, $\mathbf{C}'$ is decomposed into eigencomponents as

$$\mathbf{C}' = \lambda_1\mathbf{\Lambda}^1 + \lambda_2\mathbf{\Lambda}^2 + \lambda_3\mathbf{\Lambda}^3 \tag{8}$$

where λ_i is the i:th eigenvalue of $\mathbf{C}'$ with corresponding eigenvector $|\lambda_i\rangle$ defining $\mathbf{\Lambda}^i = |\lambda_i\rangle\langle\lambda_i|$. Assuming $\mathbf{C}'$ to be on the same form as $f_{dbl}\mathbf{C}^{dbl} + f_{sgl}\mathbf{C}^{sgl}$ it can be shown that one eigenvalue is zero, $\lambda_3 = 0$ say. The other two components can be associated to single and double bounce scattering by considering the cross-pol phase of one of the components, that is the phase of Λ^1_{13} or Λ^2_{13}. Specifically, if the phase is close to 0, the component relates to single scattering and if the phase is close to π, the component relates to double scattering. We can thus relate $f_{dbl}\mathbf{C}^{dbl}$ and $f_{sgl}\mathbf{C}^{sgl}$ to the eigencomponents as

$$Re\{\Lambda^1_{13}\} > 0 \;\Rightarrow \begin{cases} f_{sgl}\mathbf{C}^{sgl} = \lambda_1\mathbf{\Lambda}^1 \\ f_{dbl}\mathbf{C}^{dbl} = \lambda_2\mathbf{\Lambda}^2 \end{cases} \quad (9a)$$

$$Re\{\Lambda^1_{13}\} \leq 0 \;\Rightarrow \begin{cases} f_{sgl}\mathbf{C}^{sgl} = \lambda_2\mathbf{\Lambda}^2 \\ f_{dbl}\mathbf{C}^{dbl} = \lambda_1\mathbf{\Lambda}^1 \end{cases} \quad (9b)$$

3. Thirdly, the rest term is found from equation (5) as

$$\mathbf{C}^{rst} = \mathbf{C} - (f_{dbl}\mathbf{C}^{dbl} + f_{vol}\mathbf{C}^{vol} + f_{sgl}\mathbf{C}^{sgl}) \quad (10)$$

Equations (7), (9) and (10) thus yield all the separate components of equation (5), ensuring that the corresponding intensities are positive and thus representing realistic scatterers. The intensities of the components are found using equation (4) as

$$\begin{aligned} I_{dbl} &= \text{Tr}\{f_{dbl}\mathbf{C}^{dbl}\} \\ I_{vol} &= \text{Tr}\{f_{vol}\mathbf{C}^{vol}\} \\ I_{sgl} &= \text{Tr}\{f_{sgl}\mathbf{C}^{sgl}\} \\ I_{rst} &= \text{Tr}\{\mathbf{C}^{rst}\} \end{aligned} \quad (11)$$

4. DATA AND GROUND TRUTH

For this paper, we consider a scene from the NASA/JPL AIRSAR-system (no. 6830), of quad-pol data in frequency bands L and C (of wavelengths around 24 cm and 5.6 cm respectively). The scene (see figure 1) was acquired over the Beaufort sea in December 2004, flying at an altitude of 7900 meters. The angles of incidences span from 28 to 72 degrees between near and far range. However, due to pronounced noise in the far range and calibration artefacts in the near range, only incidence angles from 30 to 55 degrees are considered in this study. The azimuth and range pixel spacing is 9.26 and 6.66 meters respectively. For speckle noise reduction, the data has been processed with 118×11 looks in azimuth and range direction respectively.

A ground truth is derived following [10], using RADARSAT-1 images acquired two weeks prior to the AIRSAR mission. By comparing the AIRSAR scene to the corresponding RADARSAT-1 scene, newly formed leads are observed for which the age of ice is estimated.

Label:	Age:	Thickness:
FY1	1-2 days	9-13 cm
FY2	12-14 days	34-36 cm
FY3	>15 days	>37 cm
MY	multi-year	-

Table 1. Labels, age and estimated thickness of ice types as defined by the ground truth. All ice that is not MY ice is collectively referred to as first year (FY) ice.

In particular four classes of ice may be distinguished, of age 1 to 2 days, 12 to 15 days, 15 days to 1 year and multiple years. Using recorded temperatures in the near region and an empirical ice growth relation, the thickness of the youngest two ice types are estimated to 9-13 cm and 34-36 cm respectively. The ground truth is displayed as an overlay in figure 1, labeled according to table 1.

5. RESULTS

By applying the NNED algorithm on the scene, we get three covariance matrices (ignoring the rest component) for each frequency band and pixel. The intensity of each matrix is calculated as in equation (11), which yields three intensities per pixel. A natural way of displaying the intensities is as a RGB image, colour coded as

$$\begin{aligned} I_{dbl} &\rightarrow red \\ I_{vol} &\rightarrow green \\ I_{sgl} &\rightarrow blue \end{aligned}$$

This yields the images shown in figure 2 for L- and C-band. The intensities are displayed in decibels and the dynamic range is cropped at -27 dB and -7 dB. By visual inspection, we note that the C-band image appear more homogeneous, in particular on MY and FY3 ice. The blue-green tone in the MY ice indicates dominant single and volume scattering. Inhomogeneous structures, such as ridges, within the MY and FY3 ice appear more pronounced in L-band than in C-band. Overall, FY1-3 are dominated by single scattering, indicated by a blue tone. In the FY2 ice we do however note that the C-band image contains local regions of purple, indicating slightly stronger double bounce. It is unclear what is causing this, but possible reasons could be snow layers on the ice, mixtures of different ice types or frost flowers.

As a rough measure of the homogeneity in the intensities of each ice type, we consider the intensity histogram widths in decibels. We let the 5 and 95 percentiles define the width of each intensity histogram, ignoring intensities below -50 dB. Figure 3 shows the widths plotted as vertical bars versus the scattering types for each ice type and the mean intensities are marked with crosses. We note that the widths for C-band are narrower in all cases, except for double scattering on FY1 ice. The signal is however very weak here, below -30 dB. We also see that for the mean intensity, the single scattering component is largest in all ice types for both bands except for the MY

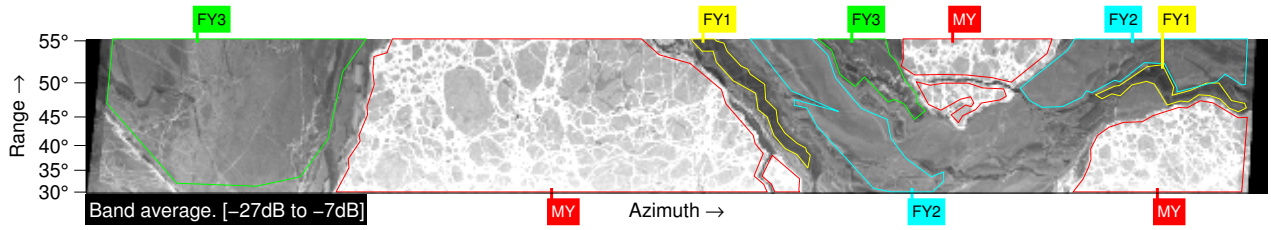

Figure 1. Total intensity averaged over both frequency bands, displayed in dB. The ground truth is overlaid and labeled according to table 1. Note that due to noise and hardware artefacts, only inclination angles from 30 to 55 degrees are considered in this paper although the full swath of the scene is 28 to 72 degrees.

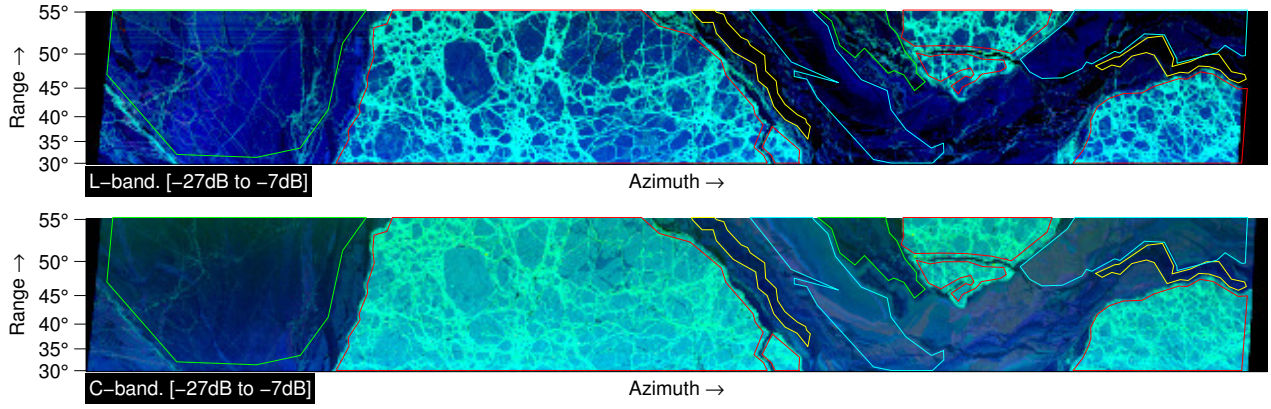

Figure 2. RGB images using the intensity of each scattering type in dB (double = red, volume = green, single = blue). As in figure 1, the ground truth is overlaid.

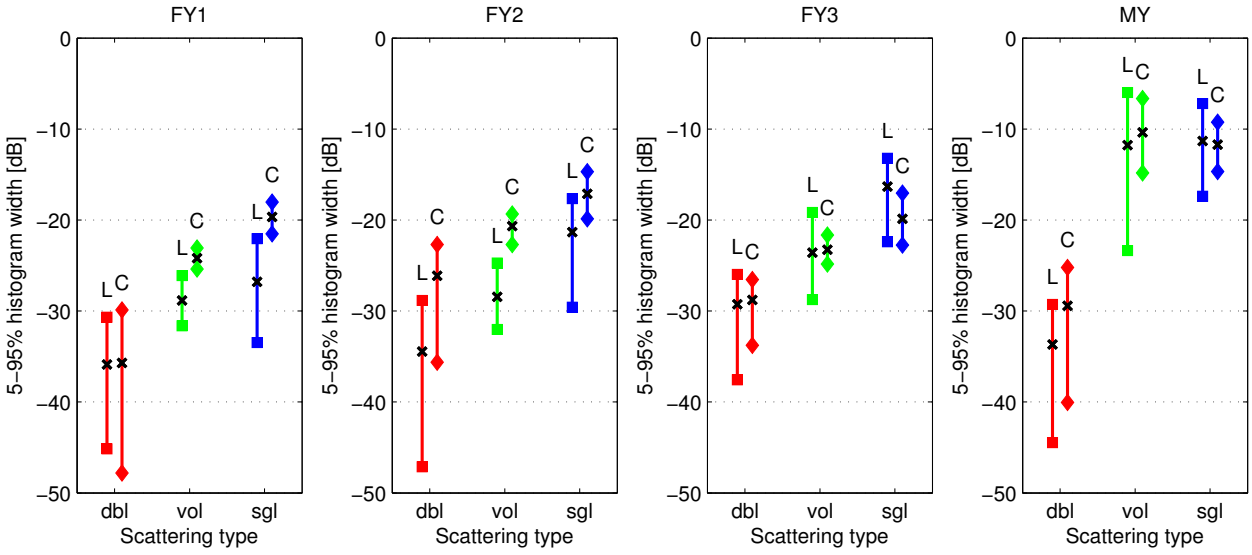

Figure 3. 5-95% intensity histogram widths versus scattering types (dbl, vol and sgl) and frequencies (L and C) plotted per ice type (FY1, FY2, FY3 and MY). The mean intensities are marked with crosses.

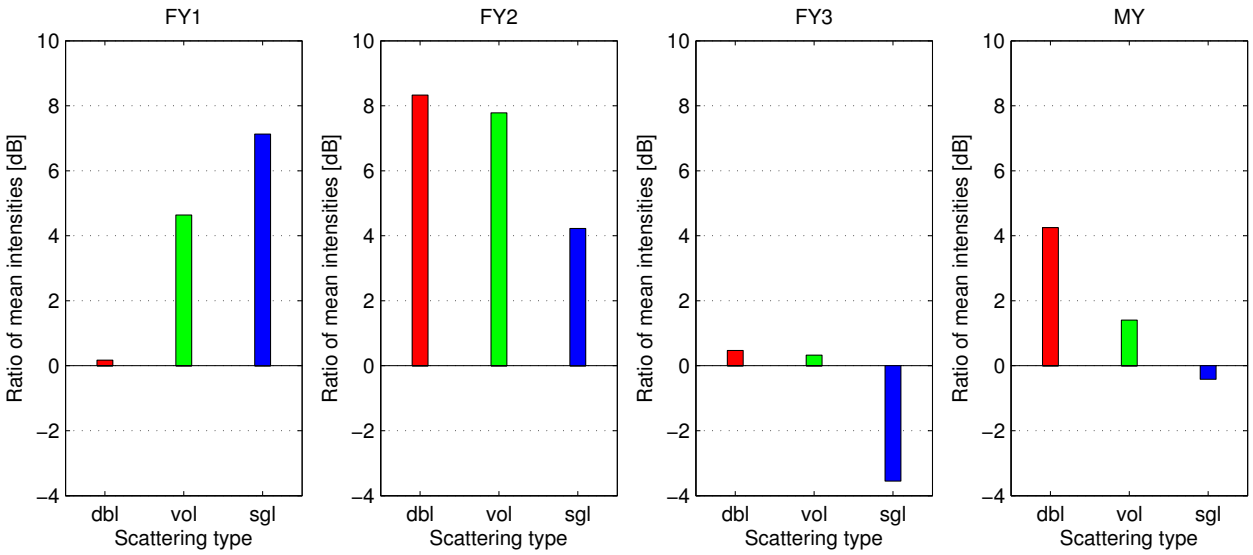

Figure 4. The ratio (or difference when expressed in dB) between mean intensities of C- and L-band. Positive values indicate that the mean intensity in C-band is greater than in L-band and vice versa.

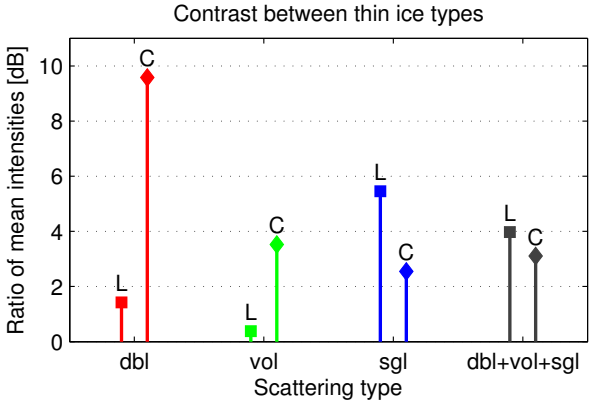

Figure 5. The ratio of mean intensity between FY1 and FY2 ice, expressed in dB.

ice, where volume scattering is comparable in strength. This is likely due to a larger amount of brine pockets and air bubbles within the MY ice compared to FY ice.

In order to further visualise the difference between the frequency bands, we compute the ratio (or difference if expressed in dB) of the mean intensities between C- and L-band. Plotting the ratios as bars for each scattering and ice type, we get figure 4. Here, a positive bar indicate that the mean intensity in C-band is greater than in L-band, whereas a negative bar indicate the opposite. The bars are aligned with the corresponding scattering and ice type in figure 3. We note that the overall difference between the bands is greatest in the FY2 ice, where C-band yield a stronger mean intensity in all scattering types. The difference is largest in the double scattering component. The greatest difference of the single component is however found in the FY1 ice, which indicate a smoother surface on the scales detected by L-band. The cases where L-band yield a stronger mean intensity, is in the single component of FY3 and MY ice, which we attribute to a larger roughness scale in these ice types than in the younger FY1 and FY2 ice.

We end the section by looking at the contrast between the thinnest ice types FY1 and FY2 per frequency band and scattering type. In particular, we compute the ratio of the mean intensity between FY1 and FY2. By expressing the ratios in decibel and taking the absolute values, we get figure 5. We note that the highest contrast is in the double component of C-band, although the signal is very weak in the FY1 ice (below -30 dB). C-band yield a higher contrast also in the volume component, but L-band dominates in the single component. Considering the sum of all scattering types, L-band yield the overall highest contrast, although C-band is comparable.

6. DISCUSSION

In this paper, we have highlighted differences between L- and C-band in terms of decomposed scattering types. We have used the NNED approach in order to ensure that the scattering types are physically realisable, yielding positive intensities. In terms of these, we have looked at differences between the frequency bands for discrimination between multi year ice and three types of first year ice of different age and thickness. We summarise the major findings as follows:

a) Overall, C-band yields a higher scattering intensity, except for single scattering in the thick first year ice, FY3 (see figure 2 and 3).

b) C-band yields a more homogeneous intensity in all ice types, except for double scattering in the very thinnest ice type FY1 (see figure 2 and 3). L-band appear favourable in detecting deformations within the ice types considered here.

c) L- and C-band differ mostly in mean intensity for the thinnest ice types, FY1 and FY2 (see figure 3 and 4). It is unclear if this is partly due to snow, ice mixture or frost flowers in the FY2 ice. However, if that is the case, a comparison between the bands or scattering types could be useful for detecting such features.

d) Overall, the relative contrast between the thinnest two ice types is larger in L-band than in C-band. However, for double and volume scattering, C-band yield a higher relative contrast (see figure 5). This indicates that it is largely a matter of choosing the right polarimetric parameters (I_{dbl}, I_{vol} and I_{sgl} in our case) rather than frequency band, in order to get a high contrast.

In summary, we see that L- and C-band differ in some key aspects and in particular for the thin ice types considered here. We conclude that L-band is favourable for detection of deformed ice. For thin ice, the choice of polarimetric parameters seems to be important.

REFERENCES

[1] Wolfgang Dierking and Henning Skriver. What is gained by using an l-band sar for sea ice monitoring? In *ENVISAT Symp., Salzburg, Austria*, 2004.

[2] Wolfgang Dierking and Jørgen Dall. Sea-ice deformation state from synthetic aperture radar imagery—part i: Comparison of c-and l-band and different polarization. *Geoscience and Remote Sensing, IEEE Transactions on*, 45(11):3610–3622, 2007.

[3] Eric Rignot and Mark R Drinkwater. Winter sea-ice mapping from multi-parameter synthetic-aperture radar data. *Journal of Glaciology*, 40(134):31–45, 1994.

[4] Jong-Sen Lee, Mitchell R Grunes, and R Kwok. Classification of multi-look polarimetric sar imagery based on complex wishart distribution. *International Journal of Remote Sensing*, 15(11):2299–2311, 1994.

[5] A Rodrigues, D Corr, K Partington, E Pottier, and L Ferro-Famil. Unsupervised wishart classifications of sea-ice using entropy, alpha and anisotropy decompositions. In *Applications of SAR Polarimetry and Polarimetric Interferometry*, volume 529, page 17, 2003.

[6] Wolfgang Dierking and Thomas Busche. Sea ice monitoring by l-band sar: An assessment based on literature and comparisons of jers-1 and ers-1 imagery. *Geoscience and Remote Sensing, IEEE Transactions on*, 44(4):957–970, 2006.

[7] Jakob J van Zyl, Motofumi Arii, and Yunjin Kim. Model-based decomposition of polarimetric sar covariance matrices constrained for nonnegative eigenvalues. *Geoscience and Remote Sensing, IEEE Transactions on*, 49(9):3452–3459, 2011.

[8] Anthony Freeman and Stephen L Durden. A three-component scattering model for polarimetric sar data. *Geoscience and Remote Sensing, IEEE Transactions on*, 36(3):963–973, 1998.

[9] Jong-Sen Lee and Eric Pottier. *Polarimetric radar imaging: from basics to applications*, volume 142. CRC PressI Llc, 2009.

[10] Daniel Bäck. Analysis of polarimetric signatures of arctic lead ice using data from airsar and radarsat. Master of science thesis, Chalmers University of Technology, Chalmers University of Technology, Göteborg, Sweden, 2007.